Journal of Zhejiang University-SCIENCE A
www.jzus.zju.edu.cn; www.springer.com/journal/11582
E-mail: jzus_a@zju.edu.cn

Research Article
https://doi.org/10.1631/jzus.A2600166

Machine learning-enabled performance prediction and operation strategy of phase-change-material-based thermal batteries

Yanyu SHEN[1,2], Linfeng ZHU[3], Ruicheng JIANG[1,3], Zhen ZHANG[3], Yuqi HUANG[1], Xiaoli YU[1], Peiwang ZHU[1,4]✉, Zhi LI[1,4]✉

[1]*College of Energy Engineering, Zhejiang University, Hangzhou 310027, China*
[2]*College of Engineers, Zhejiang University, Hangzhou 310015, China*
[3]*Zhejiang Leapmotor Technology Co., Ltd., Hangzhou 310051, China*
[4]*State Key Laboratory of Clean Energy Utilization, Zhejiang University, Hangzhou 310027, China*

Abstract: Thermal batteries based on phase change materials (PCMs) are a key technology for energy savings and carbon reduction in building heating since latent thermal energy storage by PCMs with high energy storage density indicates great potential to utilize renewable energies. However, the complicated structure of finned-tube heat exchangers and the nonlinear melting–solidification process of PCMs require a great deal of computation and time resources, highly restricting the engineering design and application of PCM-based thermal batteries. To address these issues, this study proposed a universal machine learning-enabled performance prediction framework for finned-tube PCM-based thermal batteries designed for residential domestic hot-water supply, in which thermal energy is stored in PCM during the charging process and released to cold water during the discharging process to provide usable hot water for end users. First, a simplified simulation method coupling a 1D tube model with a 3D computational fluid dynamics model is established for the rapid performance computation of thermal batteries. Second, the deep operator network framework is introduced to directly map static parameters to the time-based temperature response of outlet hot water validated by the simulation and previous experimental results. Based on the machine learning-enabled performance prediction framework, the effects of critical parameters such as tube outer diameter and thickness combination, fin distance, and flow rate on the heat storage capacity and heat release power are systematically analyzed, providing guidelines for the proposed flow rate feedback regulation strategy of thermal batteries to satisfy different usage temperatures T_{use} and time constraints. The results show that the proposed framework can accurately predict the outlet temperature and available total volume of hot-water output by thermal batteries under various conditions.

Key words: Latent thermal energy storage; Finned-tube thermal battery; Simplified simulation model; Machine learning; Operation strategy

1 Introduction

With the continuous advancement of dual-carbon goals, the large-scale integration of renewables such as solar and wind power is accelerating (Li et al., 2025; Tong et al., 2025). However, the temporal and spatial mismatch between energy supply and demand (Zhai et al., 2025) makes efficient and reliable energy storage essential for next-generation energy systems (Xie et al., 2025). Thermal energy, involved in nearly 90% of global energy conversion and utilization processes (Henry et al., 2020), offers advantages over electrochemical storage in cost, safety, and service life (Freeman et al., 2023; Abdellatif et al., 2025).

Latent thermal energy storage (LTES) is widely regarded as an effective approach for high-energy-density thermal storage (Li Z et al., 2021; Li ZR et al., 2023a). Owing to the high latent heat associated with phase change material (PCM) (Yu et al., 2023), PCM can store substantially more thermal energy than conventional sensible heat storage (Huang XY et al., 2023), exhibiting distinct advantages in applications where space is constrained or strict temperature stability is

✉ Zhi LI, liz_ym@zju.edu.cn
Peiwang ZHU, zhupw@zju.edu.cn
Yanyu SHEN, https://orcid.org/0009-0003-6905-7259
Zhi LI, https://orcid.org/0009-0007-5311-7463

Received Mar. 21, 2026; Revision accepted June 25, 2026; Crosschecked July 30, 2026

© Zhejiang University Press 2026

required (Liu et al., 2025). Numerous studies have demonstrated that LTES holds considerable potential in renewable energy load shifting (Moreno et al., 2014), waste heat recovery (Huang YP et al., 2023), and high-power thermal management systems (Christopher Selvam et al., 2025; Yan YL et al., 2026).

Although LTES possesses high energy density, its engineering application is still constrained by the low intrinsic thermal conductivity of PCM. Especially in organic phase change materials, the thermal conductivity is typically only 0.2–0.7 W/(m·K) (Liu et al., 2023; Tripathi et al., 2023), resulting in slow heat transfer and low power density. Material-level enhancement strategies have therefore been widely explored. Liao et al. (2025) developed a sodium polyacrylate/starch/disodium hydrogen phosphate dodecahydrate (PAAS/ST/DHPD) flexible phase-change hydrogel. With 65% (mass fraction) DHPD, it showed a phase-change temperature of 31 ℃, latent heat of 162.3 J/g, good thermal stability after 100 heating–cooling cycles, and compression resilience at 25 and 40 ℃. Kumar et al. (2026) prepared anisotropic shape-stable flexible composite phase change materials (FCPCMs) using paraffin wax, olefin block copolymer (OBC), styrene–ethylene–butylene–styrene (SEBS), and expanded graphite (EG). The sample with 10% (mass fraction) EG reduced the peak battery temperature by 23.5 ℃ at 4C discharge and narrowed the temperature difference by 50%. To address PCM leakage during phase transition, encapsulation and conductive fillers have also been adopted. Ebrahimi et al. (2024) proposed an in situ synthesized nanoporous nickel/graphitized-carbon foam for organic PCM encapsulation, retaining high latent heat with only an approximately 7%–12% reduction, improving shape stability, and achieving a photothermal efficiency up to about 91%. These methods have to some extent increased the thermal conductivity but may also introduce new problems, such as increased viscosity and suppressed natural convection. Li et al. (2026) proposed a slip-enhanced close-contact melting strategy using a pulse-heating layer and liquid-like slip surface, shortening the charging time from approximately 30 min to less than 3 min and achieving power densities up to about 1100 kW/m^3 while largely maintaining the energy density.

Recent studies indicate that material modification alone cannot resolve the trade-off between energy density and power density in LTES. Fin structures are widely recognized as effective passive heat-transfer enhancement methods (Elsihy et al., 2025). Properly arranged longitudinal or annular fins can enlarge the heat-transfer area and accelerate charging and discharging (Jiang et al., 2024). Accordingly, in practical engineering applications, finned-tube PCM thermal batteries are widely regarded as one of the most promising LTES configurations, thanks to their intrinsic advantages of compact structure and reliable long-term operation. Jiang et al. (2021) found that lower-shell fin placement enhanced heat conduction and natural convection, reducing melting time by up to 62% compared with the bare-tube case. Tian et al. (2024) proposed a leaf-vein-inspired self-growing fin topology with outer-tube optimization, reducing melting time by 46.4% and 57.1%, increasing specific power density by 80.6% and 125.7%, and further reducing melting time by 21.57%. Wang et al. (2024) optimized the air-side fins of plate-fin heat exchangers, increasing the comprehensive performance factor by 9.53%–22.82% and heat dissipation by 26.21% under the same pumping power. Li et al. (2023b) combined annular-fin-induced close-contact melting with nano-enhanced PCMs, reducing the melting time to approximately 52.7% of the baseline and increasing the average power density by more than 100%. Although fin structures greatly improve heat-transfer rates, the coupled effects of multiple parameters on energy and power densities still require further study.

Despite advances in material and structural optimization, the system-level coupling effects of key finned-tube parameters, including tube outer diameter, tube thickness, and fin distance, remain insufficiently understood. These parameters affect heat storage, heat release, and PCM utilization, thereby influencing both energy and power densities. Moreover, existing studies often rely on costly full-scale computational fluid dynamics (CFD) simulations or isolated parametric analyses, limiting rapid engineering design. Data-driven surrogate models have been increasingly used to replace high-fidelity simulations. Intelligent and automated operation also raises new requirements for practical PCM thermal batteries (Sun et al., 2025). Therefore, this study develops an engineering-oriented simplified whole-device model to analyze the effects of key parameters on heat-storage capacity and heat-release power. Based on experimental and simulation data, a machine-learning-based rapid prediction model

is then established. A flow rate feedback regulation strategy for residential hot-water supply is further proposed to match thermal battery performance with practical operating demands. This work provides methodological guidance for the structural design and rapid performance evaluation of PCM-integrated thermal batteries.

2 Modeling methodology

This work investigates domestic hot-water utilization scenarios, selecting a customized finned-tube PCM thermal battery as the research object to characterize its heat discharge performance. The equivalent volume of mixed hot water at the user target temperature is herein adopted as the practical evaluation index. Full descriptions of the prototype structure, material thermal properties, operational principle, and equivalent hot-water volume definition are available in Section S1 of the electronic supplementary materials (ESM).

2.1 Simplified simulation model

Due to the complex heat transfer process inside the thermal battery and the large number of grids in the computational domain, full-scale CFD simulations are computationally expensive and time-consuming. Therefore, in this study, a simplified simulation method is established. By constructing the minimum heat transfer unit, the complex heat transfer process of the cold water and the PCM is decomposed into a two-way data transfer process between the 1D tube model and the 3D CFD model. A schematic diagram of the simplified model construction is shown in Fig. 1.

Based on the periodic arrangement of the finned-tube heat exchanger, the thermal battery is decomposed into several parallel single-finned-tube units. Each unit is further divided into minimum heat-transfer units along the flow direction, representing the sequential heat exchange of cold water from inlet to outlet. Each minimum unit consists of a 1D tube model and a 3D CFD model. The 1D tube model calculates the axial temperature evolution of flowing water, while the 3D CFD model calculates the local PCM-side phase-change heat transfer. Their coupling preserves the main heat-transfer characteristics while reducing the computational cost of full-scale CFD simulations. Through the CFD simulation model, a dataset of heat flux under different inlet temperatures of the cold water and the PCM's states of charge (SOCs) is generated. The calculation for the SOC and maximum heat capacity of the 3D CFD model is as follows:

$$C_{\mathrm{SO}} = C_{\mathrm{SO,\,ini}} - \frac{\int_0^t A_{\mathrm{cold}}\, q_{\mathrm{HF}}\, \mathrm{d}\tau}{Q_{\max}}, \tag{1}$$

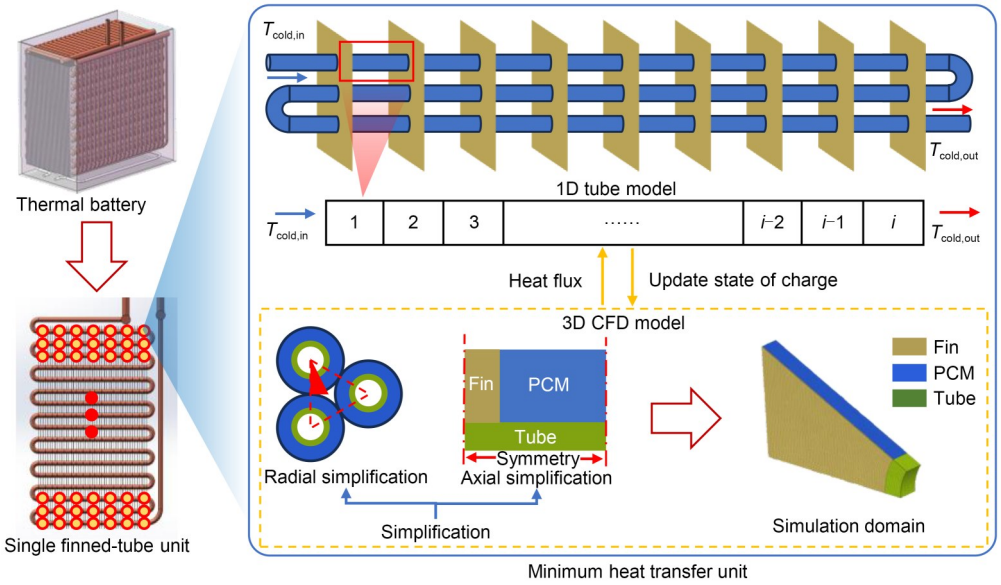


Fig. 1 Basic conception of the simplified model for thermal batteries. $T_{\mathrm{cold,in}}$ and $T_{\mathrm{cold,out}}$ denote temperatures of the cold water at the inlet and at the outlet, respectively

$$Q_{\max}=m_{\mathrm{PCM}}[\Delta h_{\mathrm{PCM}}+C_{\mathrm{p,PCM}}(T_{\max}-T_{\min})]+ m_{\mathrm{tube}}C_{\mathrm{p,tube}}(T_{\max}-T_{\min}), \quad (2)$$

where C_{SO} denotes the SOC of the PCM at time t; $C_{\mathrm{SO,ini}}$ represents the initial SOC; $Q_{\max}$ is the maximum heat storage capacity of the 3D CFD model; A_{cold} represents the heat transfer area between the cold water and the tube; q_{HF} represents the heat flux density between the cold water and the 1D tube model; m_{PCM} and m_{tube} are the masses of the PCM and the finned-tube in the model, respectively; Δh_{PCM} is the latent heat of the PCM; $C_{\mathrm{p,PCM}}$ and $C_{\mathrm{p,tube}}$ are the specific heats of the PCM and the tube, respectively; $T_{\max}$ and $T_{\min}$ are the highest and lowest temperatures during operation, respectively.

During the calculation process, the corresponding heat flux is obtained based on the SOC of the current CFD unit and the inlet temperature of the cold water, which is then loaded as input into the 1D tube model. The node outlet temperature is calculated according to the energy conservation equation, while the SOC of the current CFD unit is updated. This process continues until the outlet temperature of the last node is calculated.

2.1.1 3D CFD model

As shown in Fig. 2, the 3D simulation domain is defined by the maximum PCM range that a single finned-tube can influence and the PCM contained between two adjacent fins (Kroeger and Ostrach, 1974; Xu et al., 2024). In this study, the heat release process of the PCM within each finned-tube is similar, so it is assumed that the phase change process is uniform and symmetrical between adjacent fins (Waser et al., 2020).

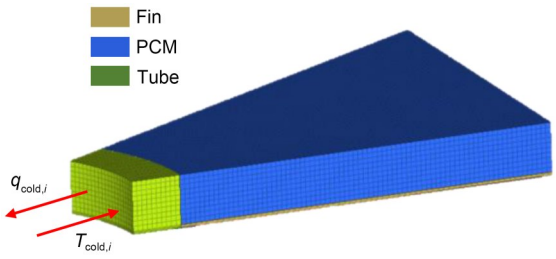


Fig. 2 Simulation domain using the finite volume method. The parameters are explained in the text

In this work, a numerical simulation model for the finned-tube PCM thermal battery is built via ANSYS Fluent. The corresponding governing equations and detailed model calculation principles are provided in Section S2 of the ESM.

2.1.2 1D tube model

Modeling the heat transfer of the cold water within the heat exchanger as a 1D tube model can reduce the time required for the fluid–solid coupling calculations in the full-scale simulation. The node discretization scheme of the 1D tube model is shown in Fig. 3. From the above simplification process, it can be seen that the number of nodes depends on the length of the single finned-tube and the number of fins (Neumann et al., 2017). Each node adheres to the principle of energy conservation, and the outlet temperature of the cold water at node i can be calculated by Eq. (3). The outlet temperature of the cold water at node i can be used to calculate the outlet temperature of the cold water at node i+1 until the last node is reached.

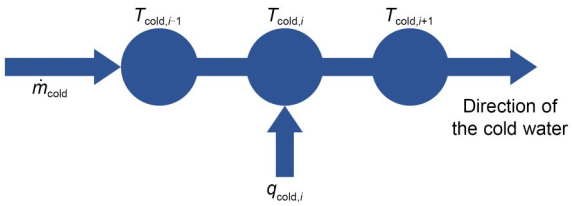


Fig. 3 Discretized node scheme of the 1D tube model

$$T_{\mathrm{cold},i}=T_{\mathrm{cold},i-1}+\frac{q_{\mathrm{cold},i}}{C_{\mathrm{p,cold}}\dot{m}_{\mathrm{cold}}}, \quad (3)$$

where $T_{\mathrm{cold},i}$ and $T_{\mathrm{cold},i-1}$ represent the outlet temperatures of the cold water at nodes i and $i-1$, respectively; $q_{\mathrm{cold},i}$ represents the heat flux fed back from the 3D CFD model to node i; $C_{\mathrm{p,cold}}$ represents the specific heat capacity at constant pressure of the cold water; $\dot{m}_{\mathrm{cold}}$ represents the mass flow rate of the cold water.

2.1.3 Model validation

This study verifies the simplified simulation model based on the thermal battery performance test bench established by Jiang et al. (2024) in our research group. The experimental method involved heating with 70 °C hot water for 2 h, letting it stand for 30 min, and then introducing cold water at room temperature to measure the temperature curve at the outlet of the thermal battery. In addition, two situations are considered: the inlet cold water temperatures are 28

and 15 °C, corresponding to the summer and winter operating conditions of the thermal battery, respectively. The results showed that the simplified simulation analysis model could maintain an error of within 10% with the experimental data most of the time.

2.2 Machine learning-enabled performance prediction model

Engineering product design and optimization impose strict limits on computational cost and efficiency. Conventional experiments are time-consuming with poor repeatability, while simplified simulation models require fixed predefined parameters and involve heavy computation. With advances in artificial intelligence, machine learning surrogate models enable rapid performance prediction of thermal batteries under various key parameters, supporting product optimization and operational strategy design.

Fig. 4 presents the machine learning workflow for thermal battery performance prediction. This work targets the prediction of time-varying outlet water temperature under different static critical parameters. Traditional artificial neural networks (ANNs) treat time as an extra input for pointwise regression and cannot capture temporal evolution patterns. Recurrent neural networks (RNNs), long short-term memory (LSTM) networks, and Transformer model support autoregressive prediction but depend on historical states and fixed time steps, making them unsuitable for static parameter-driven output prediction. In contrast, the deep operator network (DeepONet) (Lu et al., 2021), developed for operator learning, splits the temperature prediction task into branch and trunk subnetworks (Figs. 4a–4c). The branch encoder receives structural parameters (outer diameter, wall thickness, and fin distance) and the operational parameter (flow rate). The trunk network takes operating time to construct temporal basis functions. Their outputs are fused via the vector dot product to generate predictions. This framework efficiently learns the mapping between static parameters and time-dependent outlet temperatures, with strong generalization and continuous-time adaptability.

2.2.1 Data processing

In this study, the machine learning dataset is established with the thermal battery initially maintained at 70 °C (PCM fully charged), and 20 °C cold water is supplied for the heat-release process. The model output corresponds to the hourly evolution of outlet water temperature. The static input parameters adopted in

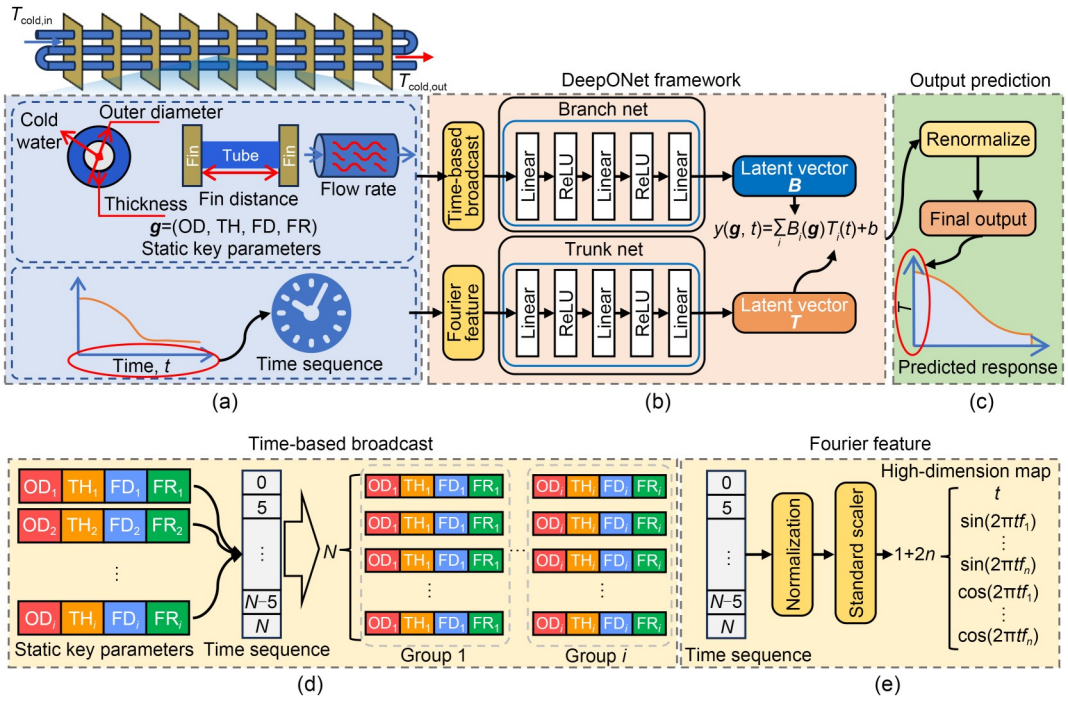


Fig. 4 Flowchart of machine learning: (a) input parameters of the model; (b) framework of DeepONet; (c) prediction performance of the model; (d) module of "Time-based broadcast"; (e) module of "Fourier feature". ReLU: rectified linear unit. The parameters are explained in the text

this work are summarized in Table 1. Considering the comprehensive heat transfer characteristics of the thermal battery, four groups of structural parameters (tube outer diameter, wall thickness, and fin distance) and the operational parameter (cold water flow rate) are selected. The diameter–thickness combinations follow commercial copper tube specifications and practical engineering standards. To guarantee engineering feasibility, the wall thickness is matched with specific outer diameters rather than varying independently.

Table 1 Input static parameters of machine learning

Parameter	Value
Outer diameter (OD, mm) and thickness (TH, mm)	6.35 and 0.8, 9.52 and 1.0, 12.70 and 1.2, 15.88 and 1.2
Fin distance (FD, mm)	2, 4, 6, 8, 10
Flow rate (FR, L/min)	6, 8, 10

Prior to model training, the input parameters are separately processed for the two DeepONet subnetworks. The trunk network receives continuous operating time and captures temporal evolution features via Fourier transformation and multilayer perceptron (MLP). As illustrated in Fig. 4e, sine and cosine functions convert time t into frequency f through Fourier series, mapping the original time information into high-dimensional frequency features, thereby constructing the time-dependent feature vector $\boldsymbol{T}(t)$. In contrast, the branch network takes a 4D static parameter vector $\boldsymbol{g}$ and compresses it into low-dimensional latent features through MLP, yielding fixed parameter embeddings $\boldsymbol{B}(\boldsymbol{g})$ for each parameter group. To realize operator learning, static parameter features are broadcast and aligned with all time points. Finally, $\boldsymbol{T}(t)$ and $\boldsymbol{B}(\boldsymbol{g})$ are combined to form the total output by performing vector dot product and adding the global bias b. As shown in Fig. 4d, each static parameter group is repeatedly matched with sequential time information, constructing complete parameter–time input pairs for subsequent temperature prediction.

2.2.2 Model training

Based on the above data processing, a total of 60 unique static parameter groups are adopted for model training. Each parameter group is broadcasted and matched with 721 time points (spanning 3600 s with a 5 s interval) to construct complete training samples. Given the limited dataset size, five-fold cross-validation is implemented to enhance model reliability and generalization. The detailed dataset settings, network hyperparameters, training configurations, and complete model validation figures are provided in Section S3 of the ESM. The results demonstrate rapid and stable model convergence, with the coefficient of determination (R^2) of both the training and test sets converging close to 1 after sufficient training, as shown in Fig. S2 of the ESM. No obvious overfitting is observed, indicating excellent fitting and generalization capability of the network. The optimal model obtained from cross-validation is further verified under multiple typical structural and operational conditions. As shown in Fig. S3 of the ESM, the predicted temperature evolutions show excellent consistency with the numerical simulation results, which validates that the proposed DeepONet model can accurately and reliably capture the dynamic heat-release responses of thermal batteries.

3 Results and discussion

For residential hot water applications, deliverable high-quality hot-water is of primary concern. Based on the simplified simulation model, this section analyses the effects of key parameters on the available V_{40} (V_{40} denotes the equivalent water volume when the user target temperature is 40 °C) under a fixed device volume. Two performance metrics are evaluated: the maximum V_{40} after full charging, representing the total heat storage capacity (energy density), and the cumulative V_{40} at different operating times until the outlet temperature drops to 40 °C, representing the instantaneous heat release capability (power density). The following parameter analysis is organized around these two metrics.

3.1 Effects of the outer diameter and thickness

Figs. 5a–5e present the outlet water temperature profiles under different tube outer diameter and thickness combinations. The temperature evolution exhibits three distinct stages: an initial rapid drop driven by sensible heat release from the finned-tubes and near-wall PCM; a plateau-like region corresponding to PCM latent heat release, during which the outlet temperature decreases slowly—note that the plateau temperature does not equal the phase-change temperature, as the outlet temperature is governed by coupled

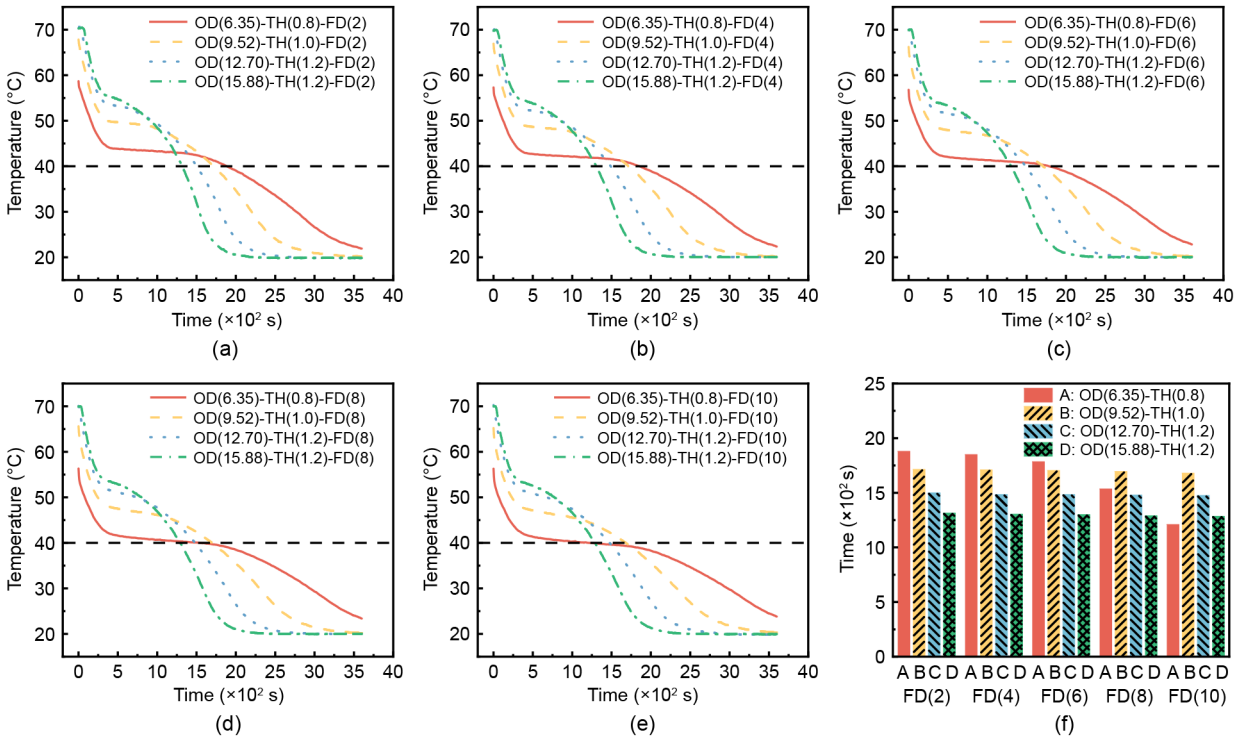


Fig. 5 Outlet water temperature of the thermal battery under different combinations of tube outer diameter and thickness: (a–e) different fin distances; (f) drop time of the outlet water temperature to 40 ℃

heat transfer among the PCMs, fins, tubes, and flow rates, and a final rapid decline after most latent heat is exhausted, entering the sensible cooling regime. At small fin distances, increasing the tube diameter raises the initial outlet temperature but shortens the heat release duration (with 40 ℃ as the threshold). For instance, the combination OD(15.88)-TH(1.2)-FD(2) achieves an initial outlet temperature of 70.25 ℃, which is 19.75% higher than that of the combination OD(6.35)-TH(0.8)-FD(2), yet its time to reach 40 ℃ is 1315 s, which is 30.05% shorter. First, with a fixed fin distance, a larger tube diameter reduces the PCM volume per finned-tube unit, facilitating initial heat transfer to cold water; simultaneously, the lower flow velocity at the same mass flow rate reduces the convective heat transfer coefficient but extends the water residence time, yielding more thorough heat exchange. Consequently, larger-diameter batteries deliver higher initial temperatures. Second, the increased tube diameter reduces the total PCM mass and thus the maximum storage capacity, preventing sustained heat release and causing the outlet temperature to drop below 40 ℃ more rapidly. This indicates that the initial-stage heat transfer resistance is dominated by the PCM itself, as heat must be gradually conducted from the interior outward.

As the fin distance increases, the heat transfer area between the PCM and tube outer wall diminishes, which disproportionately affects smaller-diameter thermal batteries. As shown in Fig. 5f, the heat release duration of smaller-diameter batteries shortens more markedly than that of larger-diameter batteries. For the combination OD(6.35)-TH(0.8)-FD(10), the time to reach 40 ℃ is 1210 s, 35.63% less than that of the combination OD(6.35)-TH(0.8)-FD(2). On the one hand, due to the reduction in fin distance, the effect of heat transfer deteriorates; on the other hand, because of the faster flow velocity, most of the PCM cannot effectively transfer the heat within itself.

The cumulative V_{40} over the full operating period is further analyzed in Figs. 6a–6e. Since cumulative V_{40} depends on both outlet temperature and operating time, smaller fin distances benefit smaller-diameter batteries: despite lower outlet temperatures, their longer heat release duration yields larger cumulative V_{40} that plateaus as operation proceeds. The maximum V_{40} (defined as the cumulative V_{40} from t=0 s until the outlet temperature drops to 40 ℃) of the combination

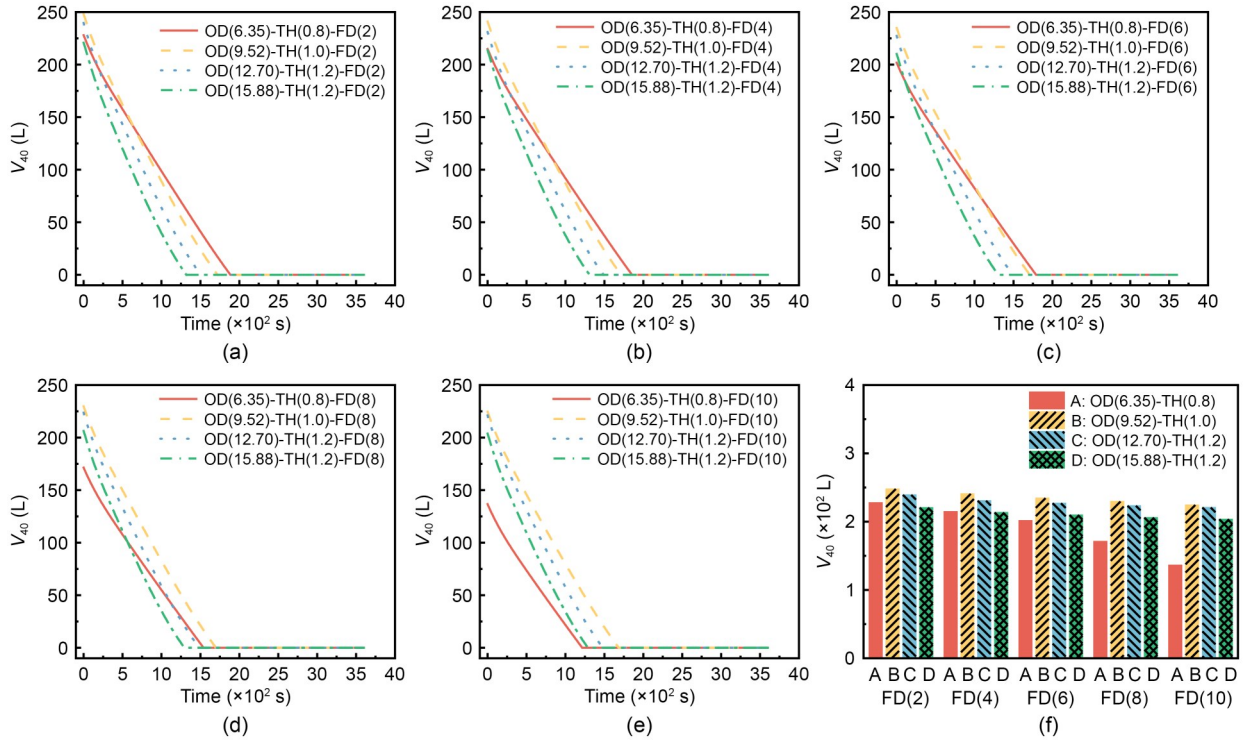


Fig. 6 Cumulative V_{40} of the thermal battery under different combinations of tube outer diameter and thickness: (a–e) different fin distances; (f) maximum V_{40}

OD(9.52)-TH(1.0)-FD(2) reaches 248.22 L, 12.4% higher than that of the combination OD(15.88)-TH(1.2)-FD(2). However, this advantage of smaller tube diameters diminishes as the fin distance increases. As shown in Fig. 6f, larger-diameter batteries not only catch up and surpass smaller ones in maximum V_{40} but also outperform them in heat release duration. The maximum V_{40} of the combination OD(6.35)-TH(0.8)-FD(10) is 136.61 L, 40.08% lower than that of the combination OD(6.35)-TH(0.8)-FD(2).

Therefore, the design of thermal battery requires careful balancing of the tube diameter and fin spacing. Smaller tube diameters extend heat release duration and can yield optimal maximum V_{40}, whereas larger tube diameters raise the initial outlet temperature at the cost of reduced maximum V_{40} and shorter heat release duration. From a thermal load management perspective, larger tube diameters enhance short-term heat release capability, making them suitable for meeting peak hot-water demand within limited time windows. Conversely, smaller tube diameters accommodate more PCMs and deliver higher maximum V_{40}, making them better suited for applications requiring prolonged heat supply and greater peak-load shifting capacity.

3.2 Effects of the fin distance

For a given tube diameter and thickness combination, the fin volume has a negligible effect on the total PCM mass due to the small fin thickness, especially compared with the impact of the tube diameter and thickness. As shown in Fig. 7, outlet water temperatures are initially similar across different fin distances but diverge after a certain point: batteries with smaller fin distances have already released most of their latent heat, whereas those with larger fin distances retain unexploited thermal energy due to reduced heat transfer area. Notably, the influence of the fin distance weakens as the tube diameter increases. Two mechanisms contribute: first, the reduced total PCM mass and smaller per-unit PCM volume around each finned-tube enable faster heat extraction; second, the lower flow velocity associated with larger diameters promotes more thorough heat exchange.

The cumulative V_{40} profiles over time are presented in Fig. 8. Consistent with the preceding analysis, smaller fin distances yield higher cumulative V_{40}, and this effect diminishes as the tube diameter increases. Notably, for larger-diameter batteries, the enhanced heat transfer from increased tube area reduces

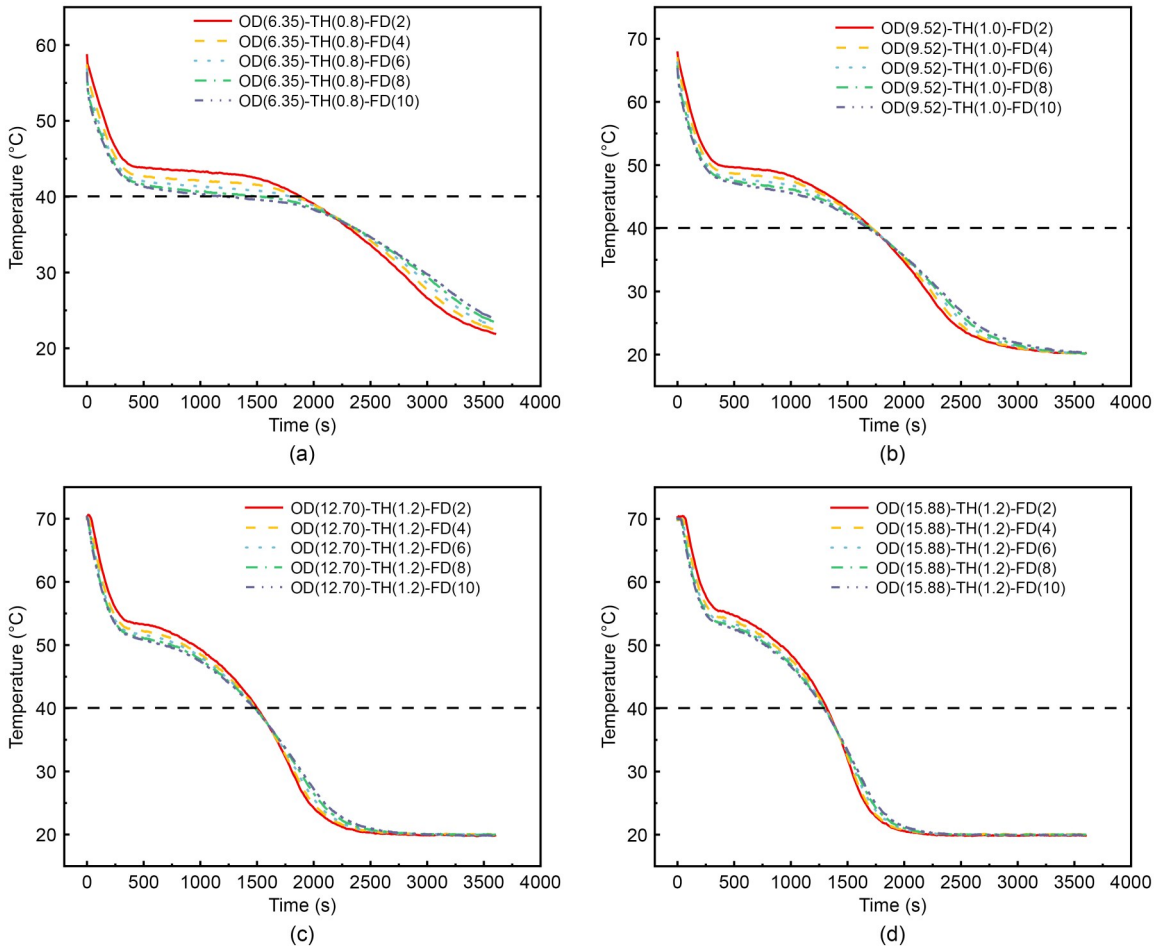


Fig. 7 Outlet water temperature of the thermal battery under different fin distances: (a–d) different combinations of tube outer diameter and thickness

the sensitivity of heat release duration to fin spacing. In contrast, the benefit of smaller fin distances is more pronounced for smaller-diameter batteries.

The influence of fin distance also reflects the trade-off between heat release rate and thermal storage capacity. A smaller fin distance enhances heat transfer and increases the available heat output within a short period, whereas a larger fin distance increases PCM loading and contributes to a greater amount of stored thermal energy. Therefore, the selection of fin distance should be based on whether the application prioritizes short-term peak demand coverage or long-term thermal load shifting.

3.3 Effects of the flow rate

For thermal batteries with identical structural parameters, V_{40} is governed by both outlet temperature and flow rate. A higher flow rate increases the convective heat transfer coefficient and instantaneous heat release power but prevents sufficient heat exchange, thereby lowering the outlet temperature. Conversely, a lower flow rate enables more thorough heat transfer and raises the outlet temperature but limits the instantaneous heat release power. These two competing effects collectively determine the net change in V_{40}.

As shown in Fig. 9, as the flow rate increases, the outlet water temperature of the thermal battery shifts downward overall. This means that even at a larger flow rate, although the convective heat transfer coefficient increases, since the heat transfer resistance is mainly concentrated within the PCM, the temperature rise of the cold water within the same time period is lower compared to that at a smaller flow rate. The initial outlet water temperature of the combination OD(6.35)-TH(0.8)-FD(2)-FR(6) can reach 58.33 °C, which is 22.96% higher than that of the combination OD(6.35)-TH(0.8)-FD(2)-FR(10).

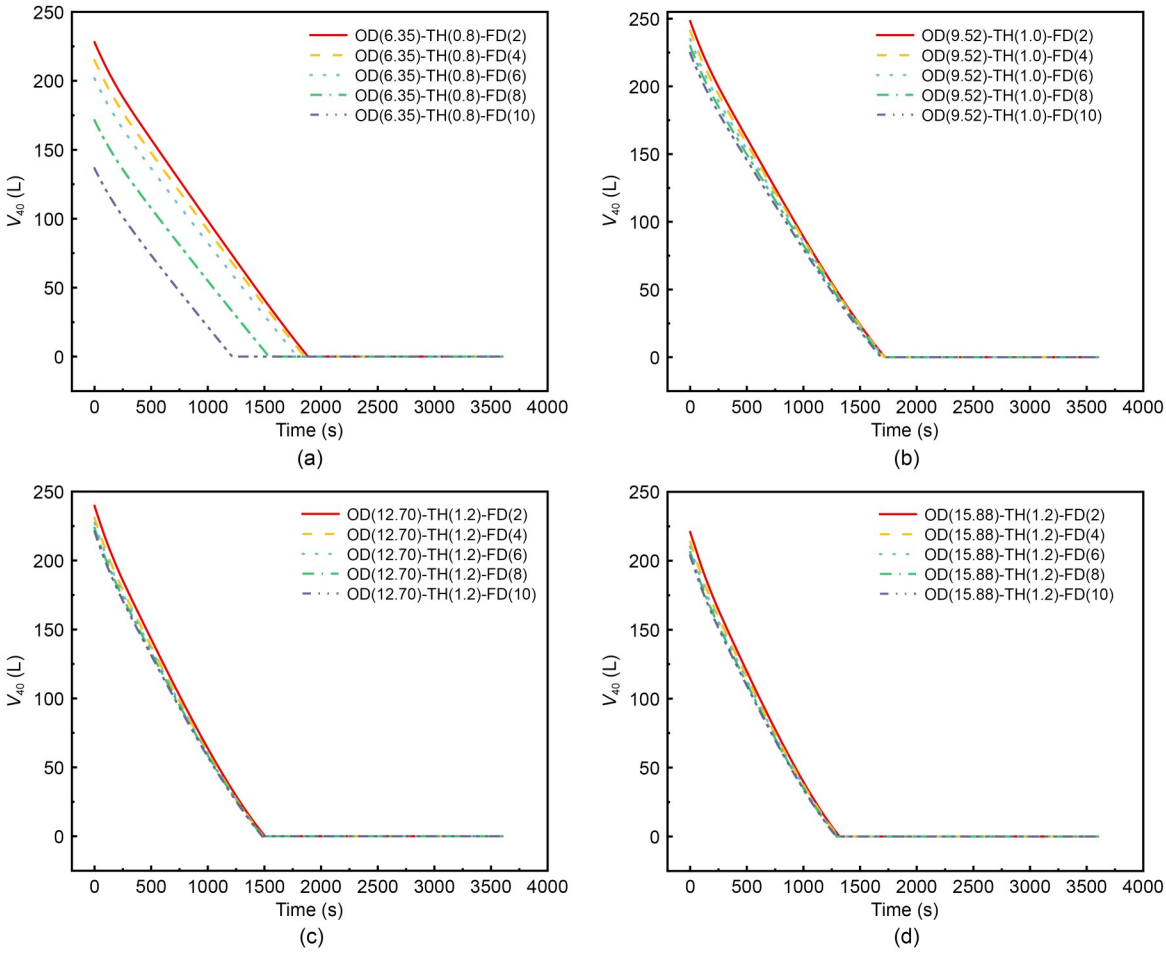


Fig. 8 Cumulative V_{40} of the thermal battery under different fin distances: (a–d) different combinations of tube outer diameter and thickness

This pattern persists throughout the entire heat release process. Notably, the influence of flow rate diminishes slightly with increasing tube diameter, which is consistent with the earlier observation that larger diameters reduce the per-unit PCM volume around each finned-tube, enabling faster heat extraction. Nevertheless, the competing relationship between outlet temperature and flow rate remains the primary determinant of V_{40}.

Cumulative V_{40} profiles under different flow rates are shown in Fig. 10. Higher flow rates do not increase the maximum V_{40}, indicating that V_{40} is ultimately limited by outlet temperature: despite higher instantaneous heat release power, the total heat extracted over the full operating period decreases, reducing the maximum V_{40}. This effect is partially mitigated by larger tube diameters, although the maximum V_{40} still declines slightly. For the combination OD(6.35)-TH(0.8)-FD(2)-FR(10), the maximum V_{40} is 32.38 L, 85.79% lower than that of the combination OD(6.35)-TH(0.8)-FD(2)-FR(6). Further analysis of the cumulative V_{40} evolution reveals that lower flow rates extend the heat release duration, requiring more time to deliver the full maximum V_{40}. Conversely, while higher flow rates yield lower cumulative V_{40} at matched time points, they release heat faster and deliver more V_{40} within equal time intervals. This highlights the need to align flow rate selection with actual user usage patterns.

The effect of the flow rate is directly related to the peak-load shifting performance of the thermal battery. Increasing the flow rate enhances the heat release power and enables a larger amount of thermal energy to be delivered within a short period. However, it also reduces the maximum V_{40} due to the shortened residence time of water inside the heat exchanger. Therefore, high flow rates are advantageous when the objective is to cover short-term peak demand, whereas lower flow rates are more suitable for maximizing the

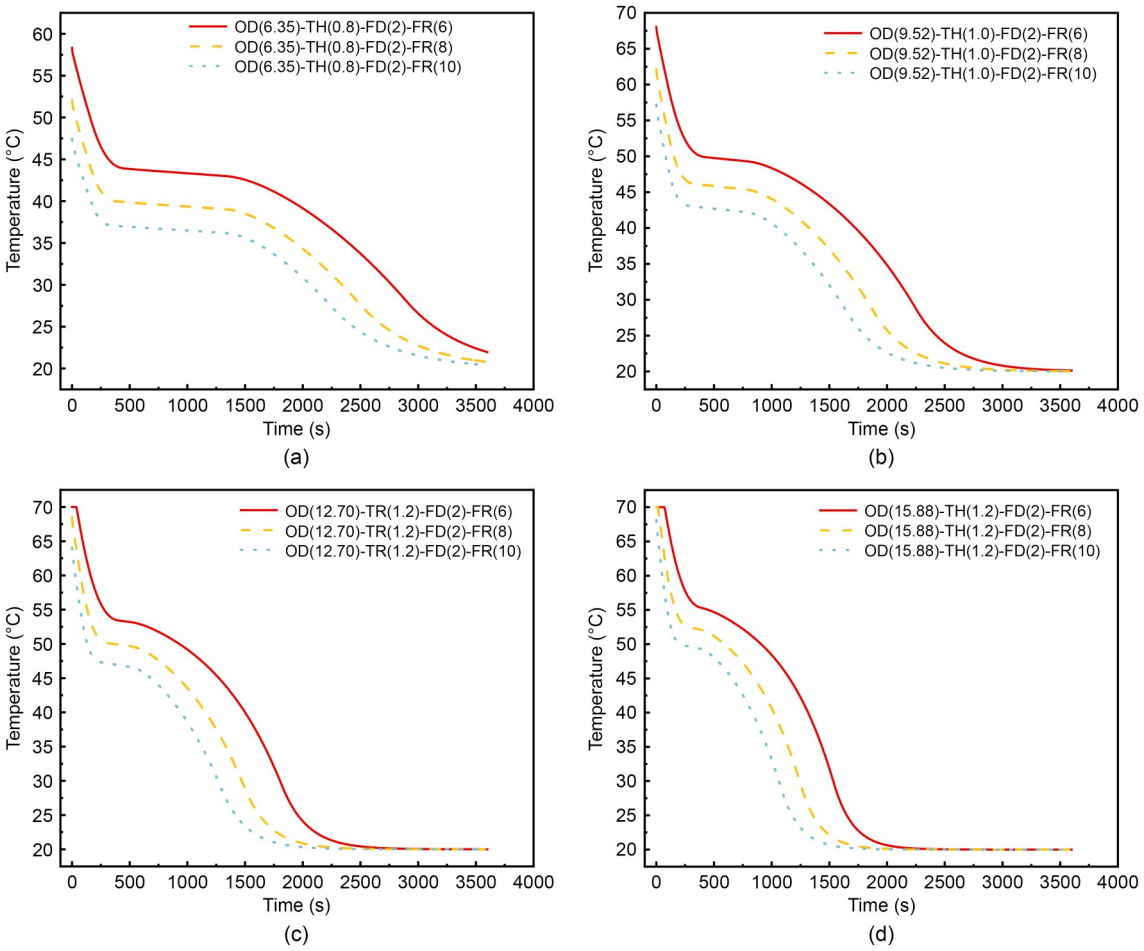


Fig. 9 Outlet water temperature of the thermal battery under different flow rates: (a–d) different combinations of tube outer diameter and thickness

utilization of stored thermal energy and extending the duration of peak-load reduction.

3.4 Feedback regulation strategy for residential hot-water supply

On the basis of analyzing the above parameters, different thermal battery structural selections are constructed for different heat demand scenarios. Choosing an appropriate combination of tube outer diameter and thickness and a smaller fin distance can achieve a larger maximum V_{40}. For rapid heat acquisition scenarios, choosing a larger tube diameter and an appropriate fin distance can achieve a shorter heat release time, meeting the immediate heat demand.

In practical applications, in addition to the design optimization for the structural selection of thermal batteries, it is also necessary to consider the resolution of the contradiction between the time and total amount of heat acquisition during the operation of the thermal battery, that is, the heat release power of the thermal battery. Therefore, based on a typical structure of a thermal battery with the parameter combination OD(12.70)-TH(1.2)-FD(2), this study proposes a heat release power regulation strategy based on intelligent flow rate feedback control, considering the different time and heat requirements of users. As shown in Fig. 11, the core of the strategy lies in the regulation of the flow rate. Specifically, the demands of users include usage temperature (T_{use}), the required time, and the equivalent water volume of the usage temperature (V_{use}). Based on the constructed thermal battery performance prediction model, the cumulative V_{use} changes can be quickly calculated. Furthermore, if the user has no limit on the usage time, then it is only necessary to compare whether the maximum V_{use} provided by the thermal battery under the current flow rate is larger than the required value. If it is larger, hot water is output; if it is less, the flow rate is reduced to increase

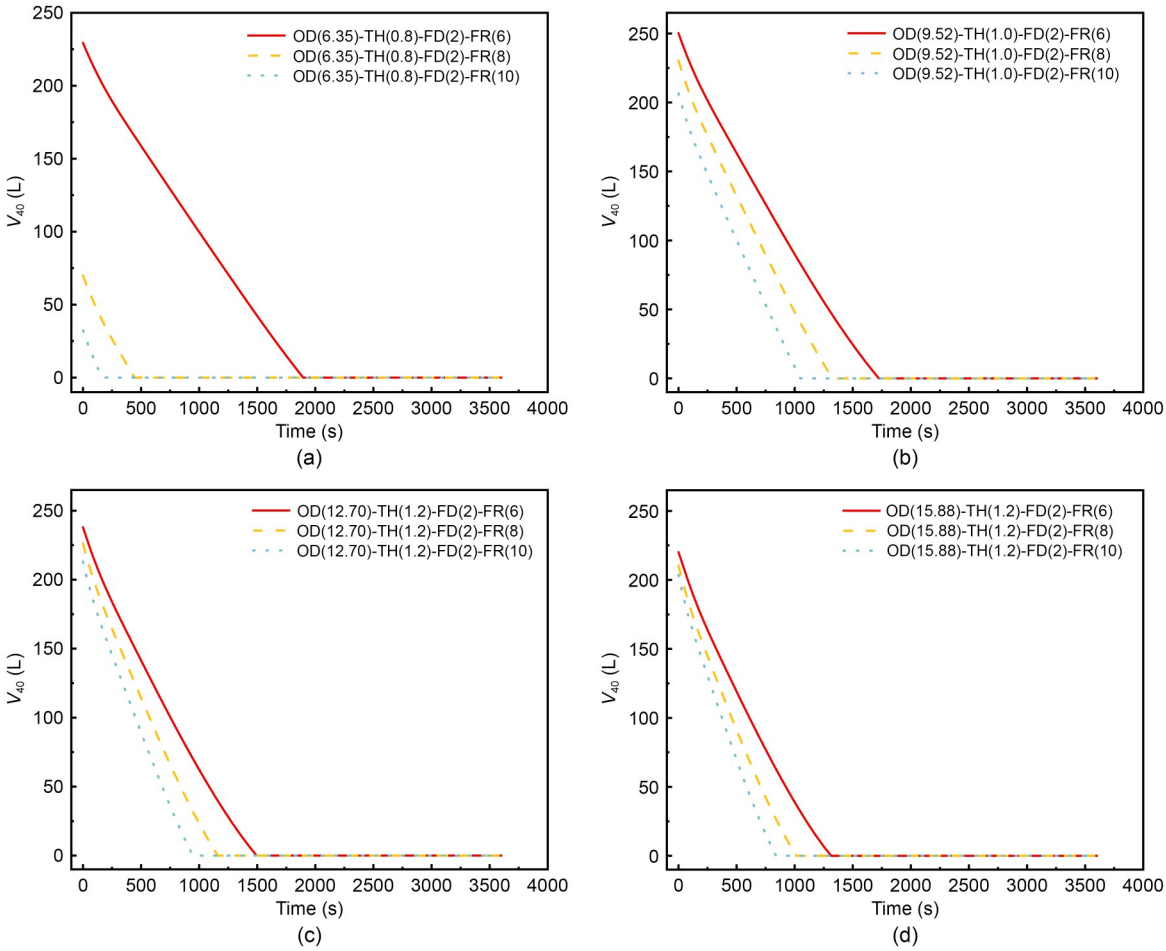


Fig. 10 Cumulative V_{40} of the thermal battery under different flow rates: (a–d) different combinations of tube outer diameter and thickness

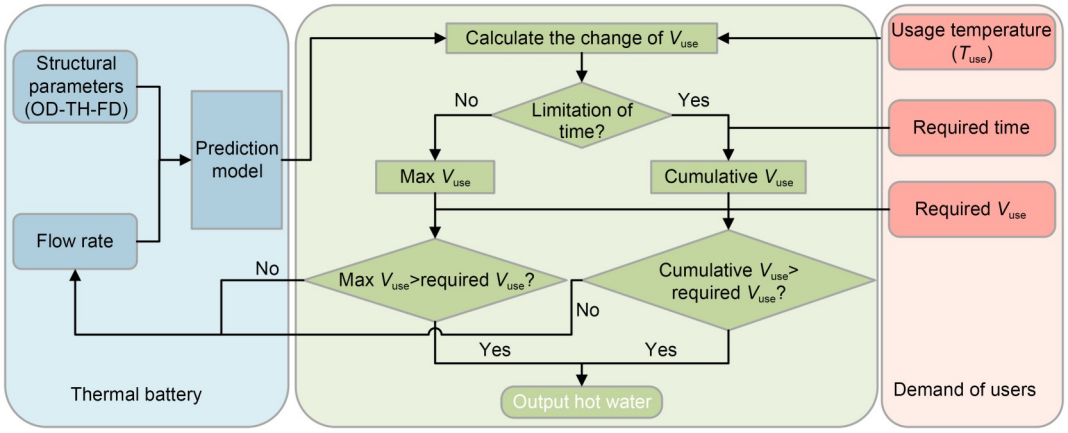


Fig. 11 Thermal battery intelligent operation strategy based on flow rate regulation

the total V_{use}. If the user has a limited usage time, then the cumulative V_{use} that can be provided within the time interval is calculated and judged whether it is larger than the required V_{use}. If it is larger, hot water is output; if it is less, the flow rate is adjusted to meet the requirements.

This study demonstrates the impact of regulating the flow rate on the cumulative V_{use} under different T_{use}

conditions, as shown in Fig. 12. Under the same T_{use} condition, as the flow rate (6.5, 7.5, and 8.5 L/min) increases, the maximum V_{use} slightly decreases, indicating a reduction in the total heat storage capacity of the thermal battery. However, when the fully charged thermal battery operates at different time intervals (10, 20, and 30 min), as the flow rate increases, the cumulative V_{use} shows an upward trend, indicating an increase in the heat release power of the thermal battery, which is consistent with the results of the above parameter analysis. As shown in Fig. 12a, at a flow rate of 8.5 L/min within 10 min, the cumulative V_{use} obtained is 13.96% higher than that at 6.5 L/min, and it can increase by 11.02% within 20 min. It is worth noting that the cumulative V_{use} obtained within 30 min is consistent with the maximum V_{use}, meaning that at this time, the thermal battery has completed the heat release of the required T_{use}, and then the outlet water temperature is lower than T_{use}.

However, as T_{use} increases (from 30 to 50 °C), as shown in Fig. 12c, due to the insufficient total heat storage capacity at higher flow rates, the maximum V_{use} decreases significantly. At a flow rate of 8.5 L/min, the maximum V_{use} decreases by up to 69.86% compared to 6.5 L/min. At this point, the heat release power at higher flow rates is limited by the maximum V_{use} and thus no longer has an advantage. It is worth noting that as T_{use} increases, due to the higher requirements for the outlet water temperature, the maximum V_{use} decreases. At a flow rate of 6.5 L/min, the maximum V_{use} at 50 °C is 80.27% lower than that at 30 °C, and the thermal energy is released over a shorter duration. At this time, it is advisable to consider connecting multiple thermal battery modules to increase the maximum V_{use} output.

These results demonstrate that the proposed prediction and regulation framework can provide guidance for balancing thermal storage capacity and heat release power according to different user demands, thereby improving the operational flexibility of residential hot-water systems.

4 Conclusions

This study proposes a machine-learning-enabled design and operation strategy for thermal batteries in residential hot-water supplies. By developing a simplified simulation model and introducing the DeepONet architecture, rapid performance prediction is achieved. Based on these models, the effects of key structural and operating parameters on high-grade hot-water supply are systematically analyzed, and an intelligent flow rate feedback regulation strategy is proposed. The main conclusions are as follows:

(1) This study establishes an efficient modeling and prediction framework to reduce the high computational cost of full-scale CFD simulations and enable rapid design iteration and time-series performance evaluation. A simplified model coupling a 1D tube model with a 3D CFD unit is developed to decompose the complex multiphysics heat-transfer process. The model maintains prediction errors within 10% while greatly reducing computational time. In addition, the DeepONet framework is introduced to directly map structural and operating parameters to the time-dependent outlet water temperature response. The five-fold cross-validation results show an R^2 approaching 1, with predictions highly consistent with simulation results, demonstrating its reliability for rapid engineering evaluation.

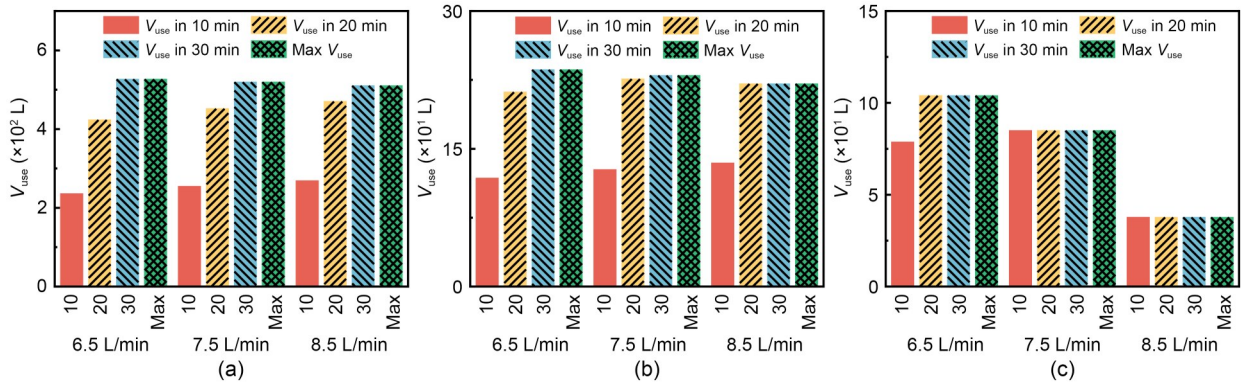


Fig. 12 Comparison of flow rate (6.5, 7.5, and 8.5 L/min) regulation under different usage temperature demands: (a) T_{use}= 30 °C; (b) T_{use}=40 °C; (c) T_{use}=50 °C

(2) This study reveals the coupling mechanisms among key structural and operating parameters, as well as the trade-off between energy density and power density in finned-tube thermal batteries. Tube outer diameter and thickness combinations, fin distance, and flow rate are selected as key parameters, while V_{40} is used to characterize high-grade hot-water release capability. Parametric analysis results show that at small fin distances, increasing the tube diameter elevates the initial outlet water temperature but shortens the heat release duration. The combination OD(15.88)-TH(1.2)-FD(2) achieves an initial outlet temperature of 70.25 ℃, which is 19.75% higher than that of the combination OD(6.35)-TH(0.8)-FD(2), yet its time to reach 40 ℃ is 1315 s, which is 30.05% shorter. The heat release duration of smaller-diameter batteries shortens more markedly than that of larger-diameter batteries. For the combination OD(6.35)-TH(0.8)-FD(10), the time to reach 40 ℃ is 1210 s, 35.63% less than that of the combination OD(6.35)-TH(0.8)-FD(2). Increasing the flow rate improves the heat release power but significantly reduces the maximum V_{40}. For the combination OD(6.35)-TH(0.8)-FD(2)-FR(10), the maximum V_{40} decreases by 85.79% compared to the combination OD(6.35)-TH(0.8)-FD(2)-FR(6), which clearly highlights the trade-off between energy density and power density.

(3) This study proposes an intelligent flow rate feedback operation strategy to resolve the dynamic mismatch between heat extraction time and total heat demand under different user scenarios for thermal batteries with fixed structures. Specifically, for a typical structural design, a regulation logic is constructed considering T_{use}, time constraints, and required V_{use}. The rapid prediction model is employed to evaluate cumulative V_{use} in real time and adjust the flow rate accordingly. The results demonstrate that in time-constrained scenarios, increasing the flow rate enhances short-term cumulative V_{use}. For example, when T_{use}=30 ℃, increasing the flow rate from 6.5 to 8.5 L/min raises the cumulative V_{use} by 13.96% within 10 min. However, under scenarios with high T_{use} requirements, higher flow rates significantly reduce the maximum V_{use}, indicating that modular expansion may be required to improve the total output capacity. This strategy provides methodological support for intelligent control in practical engineering applications of thermal batteries.

Future work should validate the proposed prediction framework and explore its application in practical thermal energy management scenarios. The developed prediction and regulation approach is expected to support intelligent operation of PCM-based thermal batteries, improve the flexibility of residential hot-water systems, and facilitate thermal load shifting and renewable energy integration in building energy systems.

Acknowledgments

This work is supported by the National Natural Science Foundation of China (Nos. 52476224 and 52206027), the Young Elite Scientists Sponsorship Program by Zhejiang Association for Science and Technology (No. ZJSKXQT2025038), and the Special Program of Hangzhou Chengxi Sci-tech Innovation Corridor, China.

Author contributions

Yanyu SHEN and Zhi LI designed the research. Yanyu SHEN, Linfeng ZHU, and Ruicheng JIANG developed the simplified simulation model and processed the corresponding data. Yanyu SHEN and Ruicheng JIANG established and validated the machine-learning prediction model. Zhen ZHANG provided engineering support for the thermal battery design and parameter settings. Yuqi HUANG and Xiaoli YU helped to organize the manuscript and prepare the figures. Yanyu SHEN wrote the first draft of the manuscript. Peiwang ZHU and Zhi LI supervised the research, revised the manuscript, and edited the final version. All authors read and approved the final manuscript.

Conflict of interest

Yanyu SHEN, Linfeng ZHU, Ruicheng JIANG, Zhen ZHANG, Yuqi HUANG, Xiaoli YU, Peiwang ZHU, and Zhi LI declare that they have no conflict of interest.

Declaration on the use of generative AI tools

No generative AI tools were used in the preparation of this manuscript.

Data availability

The data that support the findings of this study are available from the corresponding author upon reasonable request.

References

Abdellatif HE, Belaadi A, Arshad A, et al., 2025. Modeling and performance analysis of phase change materials in advanced thermal energy storage systems: a comprehensive review. *Journal of Energy Storage*, 121:116517. https://doi.org/10.1016/j.est.2025.116517

Christopher Selvam D, Devarajan Y, Beemkumar N, et al., 2025. Advances in nano-enhanced phase change materials

and hybrid thermal energy storage systems: paving the way for sustainable energy solutions. *Results in Engineering*, 27:105729. https://doi.org/10.1016/j.rineng.2025.105729

Ebrahimi M, Maleki M, Ahmadi R, et al., 2024. In-situ synthesis of nanoporous nickel/carbon composite foam to encapsulate the phase change materials for energy management. *Journal of Energy Storage*, 102:113915. https://doi.org/10.1016/j.est.2024.113915

Elsihy ES, Yuan J, Cai KT, et al., 2025. Optimizing cyclic performance of latent heat thermal energy storage systems: a comprehensive analysis of eccentricity and novel longitudinal fin geometries in shell-and-tube systems. *Energy*, 335:138211. https://doi.org/10.1016/j.energy.2025.138211

Freeman TB, Foster KEO, Troxler CJ, et al., 2023. Advanced materials and additive manufacturing for phase change thermal energy storage and management: a review. *Advanced Energy Materials*, 13(24):2204208. https://doi.org/10.1002/aenm.202204208

Henry A, Prasher R, Majumdar A, 2020. Five thermal energy grand challenges for decarbonization. *Nature Energy*, 5(9): 635-637. https://doi.org/10.1038/s41560-020-0675-9

Huang XY, Li FF, Xiao T, et al., 2023. Investigation and optimization of solidification performance of a triplex-tube latent heat thermal energy storage system by rotational mechanism. *Applied Energy*, 331:120435. https://doi.org/10.1016/j.apenergy.2022.120435

Huang YP, Deng ZL, Chen YP, et al., 2023. Performance investigation of a biomimetic latent heat thermal energy storage device for waste heat recovery in data centers. *Applied Energy*, 335:120745. https://doi.org/10.1016/j.apenergy.2023.120745

Jiang RC, Yu XL, Chang JW, et al., 2021. Effects evaluation of fin layouts on charging performance of shell-and-tube LTES under fluctuating heat sources. *Journal of Energy Storage*, 44:103428. https://doi.org/10.1016/j.est.2021.103428

Jiang RC, Qian G, Li Z, et al., 2024. Progress and challenges of latent thermal energy storage through external field-dependent heat transfer enhancement methods. *Energy*, 304:132101. https://doi.org/10.1016/j.energy.2024.132101

Kroeger PG, Ostrach S, 1974. The solution of a two-dimensional freezing problem including convection effects in the liquid region. *International Journal of Heat and Mass Transfer*, 17(10):1191-1207. https://doi.org/10.1016/0017-9310(74)90120-3

Kumar M, Sun XX, Liu SL, et al., 2026. Performance evaluation of battery thermal management system using anisotropic, shape-stable, flexible composite PCM. *Applied Thermal Engineering*, 292:130397. https://doi.org/10.1016/j.applthermaleng.2026.130397

Li Z, Lu YJ, Huang R, et al., 2021. Applications and technological challenges for heat recovery, storage and utilisation with latent thermal energy storage. *Applied Energy*, 283:116277. https://doi.org/10.1016/j.apenergy.2020.116277

Li Z, Shen YY, Fang CD, et al., 2025. Thermo-electrochemical cells enable efficient and flexible power supplies: from materials to applications. *Energy Storage Materials*, 74: 103902. https://doi.org/10.1016/j.ensm.2024.103902

Li ZR, Hu N, Fan LW, 2023a. Nanocomposite phase change materials for high-performance thermal energy storage: a critical review. *Energy Storage Materials*, 55:727-753. https://doi.org/10.1016/j.ensm.2022.12.037

Li ZR, Zhang ZK, Wang XR, et al., 2023b. Synergistic enhancement strategy on the heat charging process of a shell-and-tube thermal storage device based on close-contact melting mechanism and nano-enhanced phase change material. *Journal of Energy Storage*, 72:108529. https://doi.org/10.1016/j.est.2023.108529

Li ZR, Hu N, Wang ZB, et al., 2026. Pulse heating and slip enhance charging of phase-change thermal batteries. *Nature*, 649(8096):360-365. https://doi.org/10.1038/s41586-025-09877-0

Liao YJ, Wu X, Liu Y, et al., 2025. Development of flexible phase-change heat storage materials for photovoltaic panel temperature control. *Applied Thermal Engineering*, 259: 124909. https://doi.org/10.1016/j.applthermaleng.2024.124909

Liu CZ, Cheng QJ, Li BH, et al., 2023. Recent advances of sugar alcohols phase change materials for thermal energy storage. *Renewable and Sustainable Energy Reviews*, 188: 113805. https://doi.org/10.1016/j.rser.2023.113805

Liu L, Yu HX, Tian B, et al., 2025. A comprehensive investigation of phase change energy storage device based on structural design and multi-objective parameter optimization. *Applied Thermal Engineering*, 272:126374. https://doi.org/10.1016/j.applthermaleng.2025.126374

Lu L, Jin P, Pang G, et al., 2021. Learning nonlinear operators via deeponet based on the universal approximation theorem of operators. *Nature Machine Intelligence*, 3(3): 218-229. https://doi.org/10.1038/s42256-021-00302-5

Moreno P, Solé C, Castell A, et al., 2014. The use of phase change materials in domestic heat pump and air-conditioning systems for short term storage: a review. *Renewable and Sustainable Energy Reviews*, 39:1-13. https://doi.org/10.1016/j.rser.2014.07.062

Neumann H, Palomba V, Frazzica A, et al., 2017. A simplified approach for modelling latent heat storages: application and validation on two different fin-and-tubes heat exchangers. *Applied Thermal Engineering*, 125:41-52. https://doi.org/10.1016/j.applthermaleng.2017.06.142

Sun Z, Yao QW, Shi L, et al., 2025. Virtual sample diffusion generation method guided by large language model-generated knowledge for enhancing information completeness and zero-shot fault diagnosis in building thermal systems. *Journal of Zhejiang University-SCIENCE A*, 26(10):895-916. https://doi.org/10.1631/jzus.A2400560

Tian Y, Ji MX, Qin XL, et al., 2024. Self-growing bionic leaf-vein fins for high-power-density and high-efficiency latent heat thermal energy storage. *Energy*, 309:133086. https://doi.org/10.1016/j.energy.2024.133086

Tong ZM, Wang HD, Tong SG, et al., 2025. Thermocline performance in a molten salt thermocline energy storage tank with annular-arranged and cross-arranged diffusers. *Journal of Zhejiang University-SCIENCE A*, 26(4):339-358. https://doi.org/10.1631/jzus.A2400359

Tripathi BM, Shukla SK, Rathore PKS, 2023. A comprehensive review on solar to thermal energy conversion and storage using phase change materials. *Journal of Energy Storage*, 72:108280. https://doi.org/10.1016/j.est.2023.108280

Wang QF, Zhang SQ, Guo TP, et al., 2024. Enhancing plate-fin heat exchanger hydraulic thermal performance through air-side fin optimization based on pseudo-3D topology optimization. *Applied Thermal Engineering*, 252:123642. https://doi.org/10.1016/j.applthermaleng.2024.123642

Waser R, Maranda S, Stamatiou A, et al., 2020. Modeling of solidification including supercooling effects in a fin-tube heat exchanger based latent heat storage. *Solar Energy*, 200:10-21. https://doi.org/10.1016/j.solener.2018.12.020

Xie RY, Chen S, Zhang XJ, et al., 2025. A moisture-driven direct air capture device for low-cost gas fertilizer. *Journal of Zhejiang University-SCIENCE A*, 26(4):389-392. https://doi.org/10.1631/jzus.A2400233

Xu BS, Yang Y, Li J, et al., 2024. Computational assessment of response to fluctuating load of renewable energy in proton exchange membrane water electrolyzer. *Renewable Energy*, 232:121084. https://doi.org/10.1016/j.renene.2024.121084

Yan YL, Zhang HG, Yang FB, et al., 2026. Assessment of low-gwp refrigerants in ultra-high-temperature transcritical heat pumps: a systematic evaluation framework based on life-cycle economics. *Applied Thermal Engineering*, 291:130083. https://doi.org/10.1016/j.applthermaleng.2026.130083

Yu XL, Jiang RC, Li Z, et al., 2023. Synergistic improvement of melting rate and heat storage capacity by a rotation-based method for shell-and-tube latent thermal energy storage. *Applied Thermal Engineering*, 219:119480. https://doi.org/10.1016/j.applthermaleng.2022.119480

Zhai XR, Xu ZY, Zhang W, et al., 2025. Phase change thermal energy storage: materials and heat transfer enhancement methods. *Journal of Energy Storage*, 123:116778. https://doi.org/10.1016/j.est.2025.116778

Electronic supplementary materials

Sections S1–S3, Tables S1 and S2, Figs. S1–S3, Eqs. (S1)–(S7)